# Mid-infrared laser filamentation in molecular gases

D. Kartashov,[1,*] S. Ališauskas,[1] A. Pugžlys,[1] A. Voronin,[2,3] A. Zheltikov,[2,3,4] M. Petrarca,[5] P. Béjot,[5,6] J. Kasparian,[5] J.-P. Wolf,[5] and A. Baltuška[1]

[1]*Photonics Institute, Vienna University of Technology, Gusshausstrasse 27-387, A 1040 Vienna, Austria*

[2]*Physics Department, International Laser Center, M.V. Lomonosov Moscow State University, 119992 Moscow, Russia*

[3]*Russian Quantum Center, Novaya 100, 143025 Skolkovo, Moscow Region, Russia*

[4]*Department of Physics and Astronomy, Texas A&M University, College Station, Texas 77843-4242, USA*

[5]*Université de Genève, Chemin de Pinchat 22, 1211 Geneve 4, Switzerland*

[6]*Laboratoire Interdisciplinaire Carnot de Bourgogne, UMR 6303 CNRS-Université de Bourgogne, BP 47870 Dijon, France*

**Corresponding author: daniil.kartashov@tuwien.ac.at*

Received June 14, 2013; revised July 11, 2013; accepted July 13, 2013; posted July 17, 2013 (Doc. ID 192155); published August 15, 2013

We observed the filamentation of mid-infrared ultrashort laser pulses (3.9 μm, 80 fs) in molecular gases. It efficiently generates a broadband supercontinuum over two octaves in the 2.5–6 μm spectral range, with a red-shift up to 500 nm due to the Raman effect, which dominates over the blue shift induced by self-steepening and the gas ionization. As a result, the conversion efficiency into the Stokes region (4.3–6 μm) 65% is demonstrated. © 2013 Optical Society of America

*OCIS codes:* (320.6629) Supercontinuum generation; (320.7110) Ultrafast nonlinear optics; (320.7120) Ultrafast phenomena.

http://dx.doi.org/10.1364/OL.38.003194

Filamentation of intense ultrashort laser pulses [1,2] finds growing applications, e.g., in ultrafast photonic technologies [3] and remote sensing [4]. Efficient spectral broadening of ultrashort laser pulses in the filaments offers a promising opportunity for frequency conversion, enabling broadband spectroscopy of the atmosphere [4], UV spectroscopy of photochemical processes [5], and synthesis of sub-femtosecond pulses in the UV [6]. Filaments generated by near-IR pulses generally have very similar behaviors in molecular and atomic gases with comparable ionization potentials and nonlinear refractive indices $n_2$ (e.g., in Ar and in $N_2$, hence in air). In particular, they most often generate similar output spectra because the blue shift due to ionization and pulse self-steepening [1,2,6,7] dominates the Raman-induced red shift [8]. However, the latter can be substantial in favorable conditions [9–11].

Recently, laser sources generating high energy femtosecond pulses in the mid-IR [12] were shown to produce filaments in argon [3], generating a continuum spanning over 3 octaves. Such spectral width, also observed in a bulk crystal [13] opens new horizons in spectroscopy and remote sensing. The blue shift of the supercontinuum spectrum was attributed to ionization and self-steepening [14].

Here, we describe for the first time the filamentation of mid-IR (3.9 μm) pulses in the molecular gases $N_2$ and $O_2$, We find that the output supercontinuum spectra strongly contrast from that observed in argon [8] by displaying a clear red-shift. We interpret this red-shift as governed by enhanced Raman effect, enabling highly efficient wavelength downshift of ultrashort pulses toward mid-IR. More specifically, the filamentation of 80 fs, 10 mJ laser pulses centered at 3.9 μm in $N_2$ generates a Raman-shifted millijoule supercontinuum spanning from 2.5 to 6 μm, while filamentation in oxygen yields 65% conversion efficiency into the Stokes region (4.3–6 μm).

Experiments were performed with the optical parametric chirped-pulse amplification (OPCPA) system originally reported in [12], delivering up to 12 mJ, 80 fs (>130 GW peak power) pulses centered at 3.9 μm at the repetition rate of 20 Hz. A ≈12 mm diameter beam was focused by a $f = 2$ m spherical mirror into a 4 m-long gas cell sealed by 3 mm thick $CaF_2$ Brewster windows. The gas cell was pumped out to a pressure below $10^{-1}$ mbar and subsequently filled by a target gas. Using the $\lambda^2$ law for the critical power of self-focusing, we estimate the value of ∼200 GW for atmospheric pressure in nitrogen and oxygen. Since the estimated critical power is beyond the current capacity of the OPCPA source, the deficit of the peak power was compensated by an increase of the gas pressure in the cell.

For spectral characterization, the beam emerging from the gas cell was reflected by a pair of $CaF_2$ wedges and focused onto the input slit of the measuring device. Spectral measurements within the range from 270 to 1700 nm were performed by using a spectral analyzer (AQ-6315A, Ando) or a spectrometer (USB 4000, Ocean Optics). For spectral measurements in the mid-IR (from 2 to 6 μm), a 1/2-meter scanning monochromator (*Digikröm*, *CVI*) equipped with a liquid nitrogen cooled HgCdTe photodetector (*J15D12*, *Teledyne Judson*) was used. The spectra were merged by independently measuring the whole spectrum with a low-resolution home-built spectrometer based on $CaF_2$ prisms and a multichannel pyroelectric detector that has a flat spectral response in the spectral range of 0.35–12 μm. The longitudinal plasma distribution in the filament was characterized with two electrodes spaced by 1 cm and biased at 500 V, movable inside the cell. The current flowing between the electrodes is proportional to the electron density [15].

Injecting the mid-IR pulses into the cell filled with either $O_2$ or $N_2$ and increasing the pressure above 2 bars

 

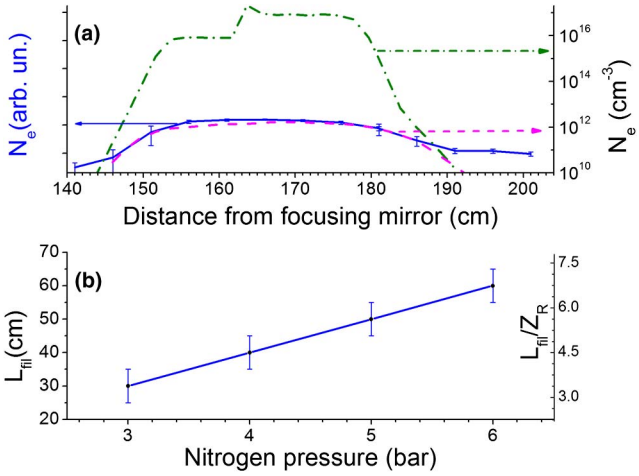


Fig. 1. (a) Longitudinal plasma distribution in nitrogen at 4 bar with an input energy of 6.5 mJ: measurements (blue line) and simulations with (magenta dashed line) and without (green dashed–dotted line) high-order Kerr effects (HOKEs). The experimental measurement is normalized to the peak of the numerical result. (b) Dependence of the filament length (foot to foot) on nitrogen pressure. The right axis shows the filament length normalized to the experimentally measured Rayleigh length $Z_R \approx 9$ cm.

resulted in a significant contraction of the output beam size, as well as ionization of the gas over a distance of several times the Rayleigh length, which is measured to lie close to $Z_R \approx 9$ cm [Fig. 1(a)]. This behavior is characteristic of filamentation, in which a dynamic balance between opposing nonlinear effects of different orders results in an efficient self-guiding. The filament length increased linearly with the gas pressure [Fig. 1(b)] up to 6 bars. Beyond that pressure, the beam structure became unstable, resulting in multiple filamentation.

As was the case in argon [14] and condensed media [13], the filamentation of mid-IR laser pulses in $O_2$ and

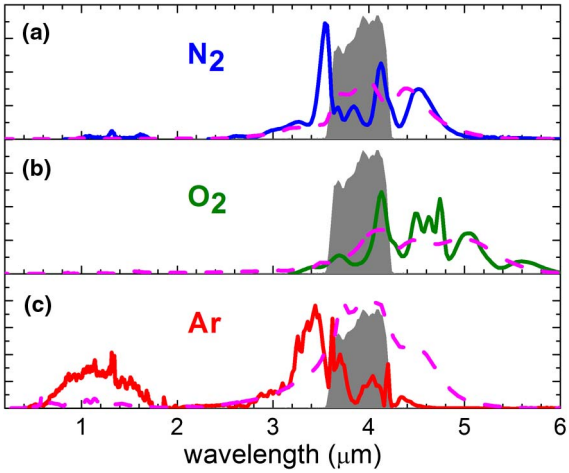


Fig. 2. (a) Blue solid line—spectrum measured after the cell filled by 4 bars of nitrogen, pulse energy 9 mJ; magenta dashed line—numerical simulations. (b) Olive solid line—spectrum measured after the cell filled by 4 bars of oxygen, pulse energy 9 mJ. Magenta dashed line—numerical simulations. (c) Red solid line—spectrum measured with 4.5 bars of Ar, pulse energy 6.5 mJ. Magenta dashed line—numerical simulations. The input spectrum is shown in all panels by the grey filled profile.

$N_2$ was accompanied by supercontinuum generation (Fig. 2), with a much more efficient broadening than in near-IR filamentation. This continuum is particularly broad in oxygen, where it spans from 3 to 6 μm at 4 bar pressure. However, while in argon the continuum was substantially blue-shifted by ~440 nm due to ionization and self-steepening [Fig. 2(c)], in molecular gases [Figs. 2(a) and 2(b)] the spectrum is red-shifted by ~500 nm (i.e., ~13% of the fundamental wavelength) in $O_2$ and by ~40 nm in $N_2$, respectively.

The difference observed between the shifts of the continuum spectra of molecular and atomic gases is remarkable, since in the near-infrared the filamentation of companion gases, featuring the same ionization potential and nonlinear refractive indices, lead to very comparable properties, including spectra. To identify the key physical processes behind these different behaviors, we solved numerically the three-dimensional field evolution equation [1,2] as detailed in Eq. (1) of Ref. [16]. It includes dispersion and absorption in a fast-ionizing molecular gas, beam diffraction, as well as the Kerr (up to the 8th order [17]), stimulated rotational Raman, and plasma nonlinearities. The field evolution equation was solved jointly with the equation for the electron density using the Keldysh model of photoionization and the Drude-type model of impact ionization with standard values of ionization potentials and electron collision times for molecular nitrogen and oxygen [1,2] The standard set of parameters fully specifying the model [1,2,18] was adapted to the mid-IR spectral range considered in this work, yielding the nonlinear refractive index coefficients $n_2 \approx 1.5 \cdot 10^{-7}(p/p_{\mathrm{atm}})$ $\mathrm{cm}^2/\mathrm{TW}$, $|n_4| < 1 \cdot 10^{-10}(p/p_{\mathrm{atm}})$ $\mathrm{cm}^4/\mathrm{TW}^2$, $|n_6| < 5 \cdot 10^{-12}(p/p_{\mathrm{atm}})$ $\mathrm{cm}^6/\mathrm{TW}^3$, and $n_8 \approx -3 \cdot 10^{-12}(p/p_{\mathrm{atm}})$ $\mathrm{cm}^8/\mathrm{TW}^4$ for $N_2$ and $n_2 \approx 3.5 \cdot 10^{-7}(p/p_{\mathrm{atm}})$ $\mathrm{cm}^2/\mathrm{TW}$, $n_4 \approx -8 \cdot 10^{-7}(p/p_{\mathrm{atm}})$ $\mathrm{cm}^4/\mathrm{TW}^2$, $n_6 \approx -1.8 \cdot 10^{-10}(p/p_{\mathrm{atm}})$ $\mathrm{cm}^6/\mathrm{TW}^3$, and $n_8 \approx -5 \cdot 10^{-12}(p/p_{\mathrm{atm}})$ for $O_2$, a standard damped oscillator model of the Raman response with an oscillation period of 390 fs for $N_2$ and 470 fs for $O_2$, decay time of 120 fs for $N_2$ and 140 fs for $O_2$, and the Raman fraction of 0.3 for $N_2$ and 0.45 for $O_2$, an ionization potential of 15.6 eV for $N_2$ and 12.1 eV for $O_2$, and the collision time in the Drude-type model of impact ionization [2] estimated as $350(p_{\mathrm{atm}}/p)$ fs for both gases. The inequalities for the $n_4$ and $n_6$ nonlinear coefficients in nitrogen mean that the contribution was found to be negligible in comparison to $n_8$. Based on the experimental spectra, showing no detectable third-harmonic signal, we infer that the cubic susceptibility responsible for third-harmonic generation is $|\chi^{(3)}(3\omega;\omega,\omega,\omega)| < 10^{-23}(p/p_{\mathrm{atm}})$ $\mathrm{cm}^2/\mathrm{V}^2$.

Numerical simulations agree well with the experimentally determined profiles of the electron density along the filament [Fig. 1(b)] and supercontinuum spectra measured at the output of the filament [Figs. 2(a) and 2(b)], thus verifying the predictive power of our model.

In order to assess the origin of the red-shift of the continuum observed at the exit of the filaments in molecular gases, we compared the solutions of the field evolution equation for supercontinuum generation by ultrashort mid-IR pulses in filament with and without the Raman term. The latter conditions cancelled the red shift (Fig. 3),

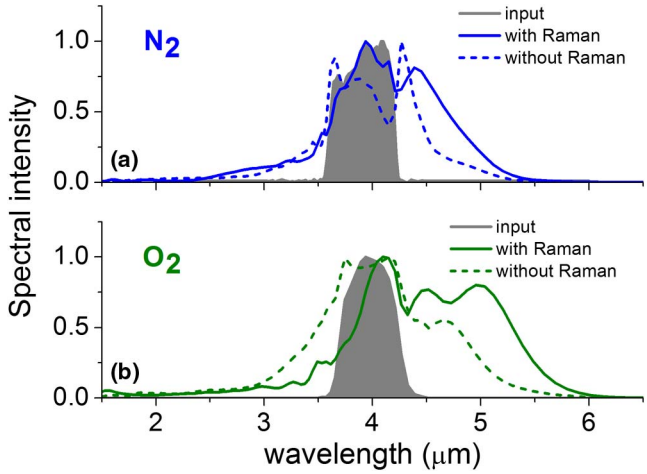


Fig. 3. Numerically calculated spectra broadening in 4 bars of (a) nitrogen and (b) oxygen without Raman contribution (dashed line) and with Raman contribution included (solid line). The gray filled profile in both panels shows the input pulse spectrum.

unequivocally illustrating the key contribution of the Raman effect. This dominant contribution also explains the different behavior of $O_2$ and $N_2$ on one side, and Ar on the other side, the latter being an atomic gas, and therefore not prone to the Raman effect. It also explains the much stronger red-shift in $O_2$ as compared to $N_2$. Since the polarizability anisotropy of oxygen is 1.6 times higher than the nitrogen one [8], the rotational torques experienced by the two corresponding molecular wavepackets under intense femtosecond field excitation are in the same ratio, so that the Raman effect contributes more to the overall nonlinearity during filamentation in $O_2$ than in $N_2$. An even stronger redshift might therefore be expected in $CO_2$, the polarizability anisotropy of which is twice that of oxygen.

Importantly, the Raman effect, accompanying filamentation of ultrashort pulses in the mid-IR, redshifts supercontinuum spectra across the entire beam [Figs. 4(a) and 4(b)], providing high overall efficiencies of wavelength downshift. This is confirmed also by spatially resolved spectral measurements with the homemade prism spectrometer. Specifically, the red-shifted part of the filament output spectrum (4.3–6 μm) in oxygen [Fig. 2(b)] carries about 65% of the input laser energy, providing a millijoule source of mid-IR pulses with wavelengths extending down to 6 μm.

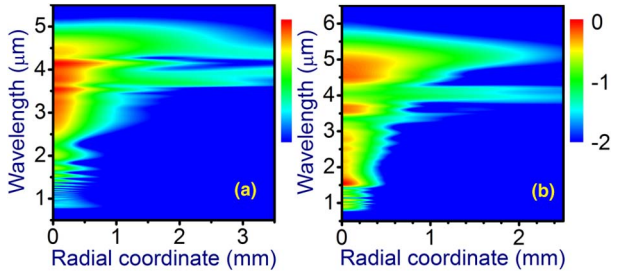


Fig. 4. Supercontinuum distribution over the beam at the output of a cell with (a) $N_2$ and (b) $O_2$ at $p = 4$ atm for an input pulse width of 80 fs and an initial energy of 9 mJ.

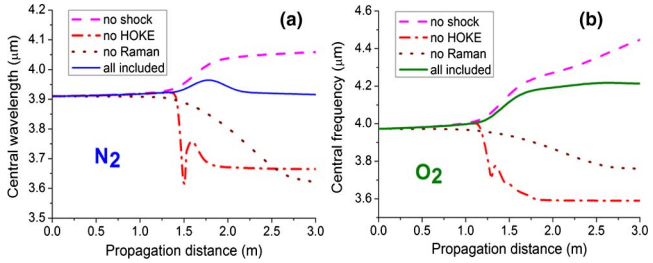


Fig. 5. Central wavelength of a mid-IR laser pulse with an input pulse width of 80 fs and an initial energy of 9 mJ as a function of propagation distance in (a) molecular nitrogen and (b) molecular oxygen, both at $p = 4$ atm, simulated using the full model with all the relevant effects included (blue and green solid line correspondingly), without HOKEs (red dashed–dotted line), without the shock term (magenta dashed line), and without the Raman effect (the bordeaux dotted line).

This result is in striking contrast with the laser-induced filamentation in the near-IR, where Raman-induced red shift is usually masked or suppressed by spectral blue shift due to ionization and where ionization leads to a considerable energy loss. In the mid-IR spectral range, higher-order nonlinear susceptibilities play much more significant role [18], clamping the field intensity in a filament at much lower levels (e.g., 33 TW $\cdot$ cm$^{-2}$ in 4 bar $N_2$, versus 160 TW $\cdot$ cm$^{-2}$ if higher-order susceptibilities were disregarded) and ionization effects are too weak [typical electron densities being well below $10^{13}$ cm$^{-3}$, see Fig. 1(b)] to give rise to any noticeable energy losses or spectral shifts. Subsequently the efficiency of the Raman term dominates the other nonlinear terms inducing spectral shifts of the supercontinuum by a factor of 2, so that the associated red shift of the supercontinuum generated in a filament becomes very high. This feature, specific to the mid-IR and to molecular gases, suggests an attractive practical scheme for wavelength down-conversion in the molecular fingerprint region.

In Figs. 5(a) and 5(b), we examine the dynamics of the wavelength shift of the mid-IR pulse in a filament in molecular nitrogen and oxygen, respectively. In the absence of high-order Kerr effect (HOKE), the wavelength shift in both gases is dominated by ionization-induced blue shift. The HOKE in the studied range of parameters tends to limit the field intensity and the electron density in a filament. With the HOKEs included in the model, the overall wavelength shift is controlled by the interplay of the Raman-effect-induced red shift and the blue shift due to the shock-type self-steepening of the laser pulse. In molecular nitrogen, these two effects are seen to effectively cancel each other for propagation paths longer than 2 m. in molecular oxygen, on the other hand, a stronger Raman effect prevails over the shock-induced blue shifting, giving rise to a pronounced red shift, which tends to accumulate with the propagation distance. The compressibility of the broadband mid-IR field waveform produced at the output of a filament is demonstrated by the results of simulations presented in Fig. 6. Here, we show that chirp compensation with a 1.6 mm $CaF_2$ plate with no additional nonlinear phase shifts can compress the supercontinuum output of a filament (blue dotted line in Fig. 6) to an FWHM pulse width of 15 fs (magenta solid

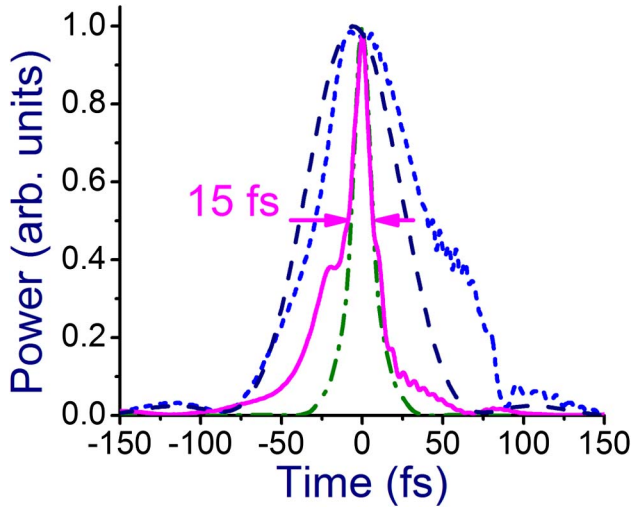


Fig. 6. Simulation of temporal envelopes of the Mid-IR laser output (dark blue dashed line), the pulse behind the gas cell with $N_2$ at 4 bar (blue dotted line), compressed pulse behind a 1.6 mm-thick $CaF_2$ plate (magenta solid line), and transform-limited pulse supported by the entire spectrum bandwidth generated in the filament inside the gas cell (green dashed–dotted line).

line in Fig. 6). The transform-limited FWHM pulse width (green dashed–dotted line in Fig. 6) supported by the entire spectrum bandwidth generated in the filament inside the $N_2$ cell is only 10% shorter than the FWHM duration of the pulse compressed by the $CaF_2$ plate. However, the uncompensated phase distortions of this pulse are seen to give rise to a prepulse and postpulse containing 23 and 9% of the overall energy of the laser pulse, respectively.

To summarize, filamentation of mid-infrared (3.9 μm) ultrashort (10 mJ, 80 fs) pulses has been observed in molecular gases. It gives rise to a spectacular supercontinuum generation together with efficient wavelength downconversion due to the domination of the Raman term over the ionization and self-steepening ones usually responsible for a spectral blue shift. The conversion efficiency into the red part of the continuum (4.3–6 μm) therefore reaches up to 65%.

This work was partially supported by the Seventh European Framework Programme (CROSS TRAP 244068 project). J. P. W acknowledges financial support from the ERC advanced grant "FilAtmo." P. B. acknowledges financial supports from the Conseil Régional de Bourgogne (FABER program), the CNRS, and the LABEX ACTION (contract ANR-11-LABX-01-01). A. V. and A. Z. acknowledge a partial support of their research by the Russian Foundation for Basic Research, the Welch Foundation (grant no. A-1801), and Skolkovo Foundation (grant no. 78).

**References**

1. L. Bergé, S. Skupin, R. Nuter, J. Kasparian, and J.-P. Wolf, Rep. Prog. Phys. **70**, 1633 (2007).
2. A. Couairon and A. Mysyrowicz, Phys. Rep. **441**, 47 (2007).
3. C. Hauri, A. Guandalini, P. Eckle, W. Kornelis, J. Biegert, and U. Keller, Opt. Express **13**, 7541 (2005).
4. J. Kasparian, M. Rodriguez, G. Méjean, J. Yu, E. Salmon, H. Wille, R. Bourayou, S. Frey, Y.-B. André, A. Mysyrowicz, R. Sauerbrey, J.-P. Wolf, and L. Wöste, Science **301**, 61 (2003).
5. T. Fuji, T. Horio, and T. Suzuki, Opt. Lett. **32**, 2481 (2007).
6. F. Reiter, U. Graf, E. E. Serebryannikov, W. Schweinberger, M. Fiess, M. Schultze, A. M. Azzeer, F. Krausz, A. M. Zheltikov, and E. Goulielmakis, Phys. Rev. Lett. **105**, 243902 (2010).
7. E. Goulielmakis, S. Koehler, B. Reiter, M. Schultze, A. J. Verhoef, E. E. Serebryannikov, A. M. Zheltikov, and F. Krausz, Opt. Lett. **33**, 1407 (2008).
8. T. Seideman, J. Chem. Phys. **103**, 7887 (1995).
9. Y. Chen, F. Théberge, C. Marceau, H. Xu, N. Aközbek, O. Kosareva, and S. L. Chin, Appl. Phys. B **91**, 219 (2008).
10. E. T. J. Nibbering, G. Grillon, M. Franco, B. Prade, and A. Mysyrowicz, J. Opt. Soc. Am. B **14**, 650 (1997).
11. A. C. Bernstein, J.-C. Diels, T. S. Luk, T. R. Nelson, A. McPherson, and S. M. Cameron, Opt. Lett. **28**, 2354 (2003).
12. G. Andriukaitis, T. Balčiūnas, S. Ališauskas, A. Pugžlys, A. Baltuška, T. Popmintchev, M.-C. Chen, M. M. Murnane, and H. C. Kapteyn, Opt. Lett. **36**, 2755 (2011).
13. F. Silva, D. R. Austin, A. Thai, M. Baudisch, M. Hemmer, D. Faccio, A. Couairon, and J. Biegert, Nat. Commun. **3**, 807 (2012).
14. D. Kartashov, S. Ališauskas, A. Pugžlys, A. Voronin, A. Zheltikov, M. Petrarca, P. Béjot, J. Kasparian, J.-P. Wolf, and A. Baltuška, Opt. Lett. **37**, 3456 (2012).
15. S. Henin, Y. Petit, D. Kiselev, J. Kasparian, and J.-P. Wolf, Appl. Phys. Lett. **95**, 091107 (2009).
16. A. A. Voronin, S. Ališauskas, O. D. Mücke, A. Pugžlys, A. Baltuška, and A. M. Zheltikov, Phys. Rev. A **84**, 023832 (2011).
17. P. Béjot, J. Kasparian, S. Henin, V. Loriot, T. Vieillard, E. Hertz, O. Faucher, B. Lavorel, and J.-P. Wolf, Phys. Rev. Lett. **104**, 103903 (2010).
18. D. Kartashov, S. Ališauskas, A. Pugžlys, A. A. Voronin, A. M. Zheltikov, and A. Baltuška, Opt. Lett. **37**, 2268 (2012).